Supporting Information for: Spin-State dependent Conductance Switching in Single Molecule-Graphene Junctions

Enrique Burzurí,[*,†,‡] Amador García-Fuente,[¶] Victor García-Suárez,[¶] Kuppusamy Senthil Kumar,[§,‖] Mario Ruben,[§,‖] Jaime Ferrer,[*,¶] and Herre S. J. van der Zant[⊥,‡,#]

†*Kavli Institute of Nanoscience, Delft University of Technology, 2600 GA Delft, The Netherlands*

‡*IMDEA Nanoscience, Ciudad Universitaria de Cantoblanco, c/Faraday 9, 28049 Madrid, Spain*

¶*Departamento de Física, Universidad de Oviedo and CINN (CSIC), ES-33007 Oviedo, Spain*

§*Institut of Nanotechnology, Karlsruhe Institute of Technology (KIT), D-76344 Eggenstein-Leopoldshafen, Germany*

‖*Institute de Physique et Chimie de Materiaux de Strasbourg (IPCMS), UMR 7504, CNRS-Universite de Strasbourg, F-67034 Strasbourg, France*

⊥*Kavli Institute of Nanoscience, Delft University of Technology, PO Box 5046, 2600 GA Delft, The Netherlands*

#*Departamento de Física de la Materia Condensada and Condensed Matter Physics Center (IFIMAC), Universidad Autónoma de Madrid, E-28049 Madrid, Spain*

E-mail: e.burzurilinares@tudelft.nl; j.ferrer@cinn.es

This supporting information is divided in three sections. Section 1 contains additional details on the geometry and dimensions of the electrodes and a representative electronic characterization of the empty few-layer graphene (FLG) electrodes. Section 2 contains additional examples of FLG|Fe-SCO|FLG junctions. Finally, Section 3 contains more details of the DFT and quantum transport simulations, including the projection of the density of states on the different molecular orbitals.

1.Geometry and characterization of empty FLG junctions

1.1. Geometry and dimensions of the FLG devices. Molecular deposition.

A thorough description of the fabrication of the FLG electrodes as well as a set of images of the devices can be found in Ref.[1] . In summary, a micron-size flake is selected under the optical microscope to fabricate the FLG electrodes. Gold pads are deposited thereafter on the flake to create electrical access. Parts of the flake are etched away with oxygen plasma so that a pre-patterned bridge of approximately 100-200 nm width is formed as seen in Figure 1 of the main manuscript. Additional atomic force microscopy (AFM) images are shown in Figure S1. The gap separating source and drain electrodes is opened by feedback-controlled electroburning. The burning process typically starts around the middle segment of the bridges' edges as explained in Ref.[1] . The minimum separation between the electrodes, 1-2 nm, is localized in a small section of the gap where the last contact point before total electroburning was placed. The remaining sections of the electrodes edges can be separated tens of nanometers apart.

Once the electrodes are prepared, the SCO molecules are dispersed in a 10^{-4} M solution of acetonitrile. A droplet is drop-casted on the chip and thereafter dried with N_2 gas. A

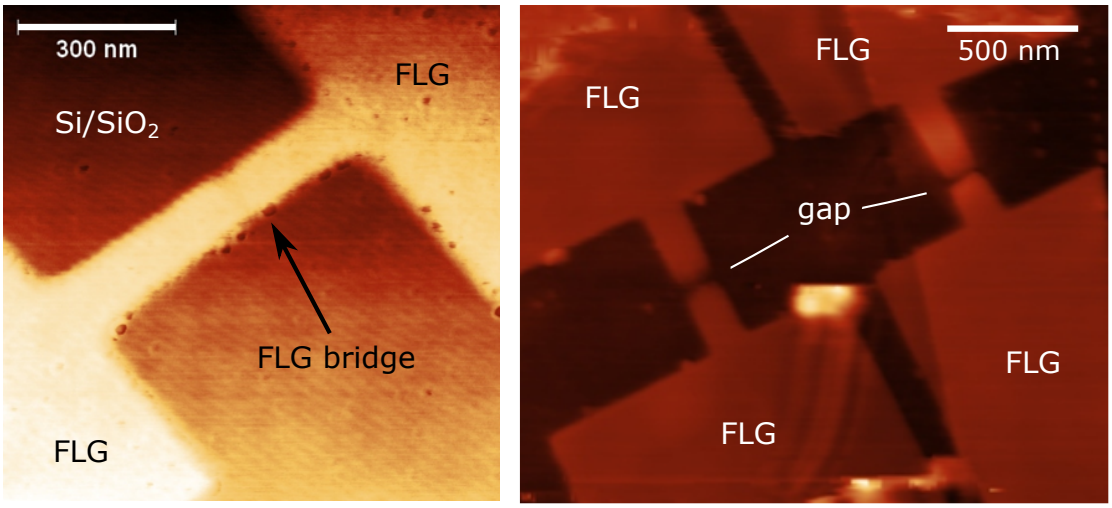

Figure S1: Atomic force microscopy (AFM) images of several FLG devices after pre-patterning with a combination of electron-beam lithography and oxygen plasma etching.

low concentration is chosen on purpose to reduce the probability that a given device has its electrodes bridged by more than one molecule. Furthermore, only those molecules that are deposited at the effective gap section can bridge the electrodes.

We note that only 10% of the samples contain molecular traces, so the probability that one molecule bridges the electrodes is $P_1 \approx 0.1$. This value is comparable to other studies using electromigrated Au,[2] or electroburned graphene electrodes.[3] This spells that the probability of finding two molecules bridging a junction is $P_2 = P_1^2 \approx 0.01$, if the two events are statistically uncorrelated, so that only one in one hundred samples should have more than one molecule. In addition, steric hindrance among molecules should reduce P_2 below 0.01. As a consequence, we expect that the probability that one of our samples contain more than one molecule is low.

In the unlikely scenario of more than one molecule in the gap and bridging the electrodes, the electron-transport across the junction would be dominated by the one more strongly coupled to the electrodes. In the even more unlikely circumstance that two molecules are present with equivalent couplings, three different current values should be observed for switching molecules ($2I_{min}$, I_{min}+I_{max}, $2I_{max}$) given that the molecules switch incoherently. The latter is ruled out in our experiments. Our conclusions remain trivially the same if they switch

coherently.

1.2. Characterization of the empty gap

Figure S2 shows the current (I) - voltage (V) characteristic measured between a pair of FLG electrodes (sample 6) before (empty electrodes) and after deposition of a solution with the Fe-SCO molecules. The high-bias current increases around two orders of magnitude after molecular deposition pointing to the formation of a molecular junction.[1,3] The low-bias conductance gap is consistent with the large-gap (LG) state observed in the other samples and with the Fe-SCO molecule in a LS state according to DFT calculations.

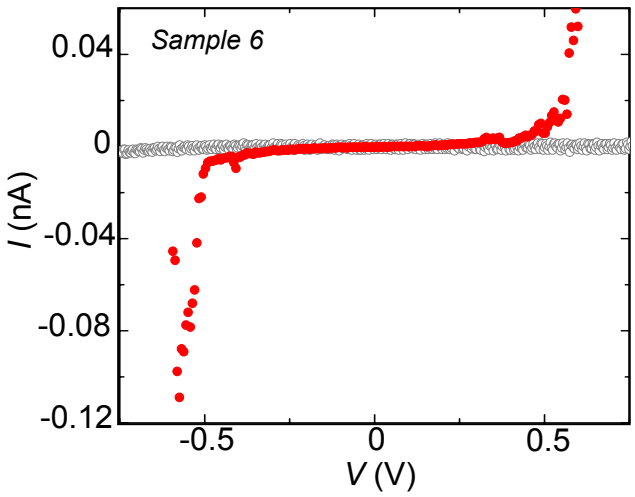

Figure S2: Current versus bias voltage measured across a pair of nanometer-spaced FLG electrodes (sample 6) before (gray empty dots) and after (red full dots) deposition of the Fe-SCO molecules. The high-bias current increases around two orders of magnitude indicating the formation of a molecular junction.

1.3. Charge offset effects

Charge-offsets can lead to abrupt shifts in the current but these are, however, typically "seen in" and "activated by" sweeping the gate voltage. In contrast, our measurements show time-dependent switching at a fixed gate voltage. Furthermore, the switching rate associated with

thermally-activated hoping of charges from charge trap to charge trap would be strongly temperature dependent. In contrast, we do not observe a strong temperature dependence of the switching in Figure 3(a) in the main manuscript. Deep traps may still be present and activated by an electrical field. However, the randomness we see in the switching rates (both in time and bias voltage) together with the reproducibility of the threshold voltages mentioned before do no support such a picture.

2. Additional samples

Figure S3(a) shows an I - V characteristic measured at $T = 100$ K in an additional junction (sample 4) containing an Fe-SCO molecule. The high-bias current and the size of the low-bias suppression gap fit well with the SG state characteristics of samples 1, 2 and 3 shown in Figure 2 of the main manuscript. Following the rationale provided by DFT, the Fe-SCO molecule is in a high-spin (HS) state as explained in Figure 4(b) of the main manuscript. In contrast to samples 1 to 3, no conductance bistability or switching between different conductance states is observed in this junction. The time stability of this sample is plotted in Figure S3(b), showing that the molecule is locked in the small-gap state. This different behavior could be explained for a molecule that undergoes relatively larger deformations between the electrodes ($\Delta r > 2.5\%$). Small perturbations can in that case not modify the ligand distance enough to induce the spin crossover transition (see Figure 4(c) in the main manuscript).

Figure S3(c) shows an I-V characteristic measured on sample 5 of which the time trace is shown in Figure 3 of the main text. The low-bias conductance gap is consistent with the SG state and therefore with the HS state. The high-bias current shows negative differential conductance. We discuss this in the next subsection. Figure S3(d) shows a 2D I *versus* V histogram made with approximately 10^4 current traces measured over time. Two bistable conductance states, corresponding to the LG and the SG states can be observed consistent

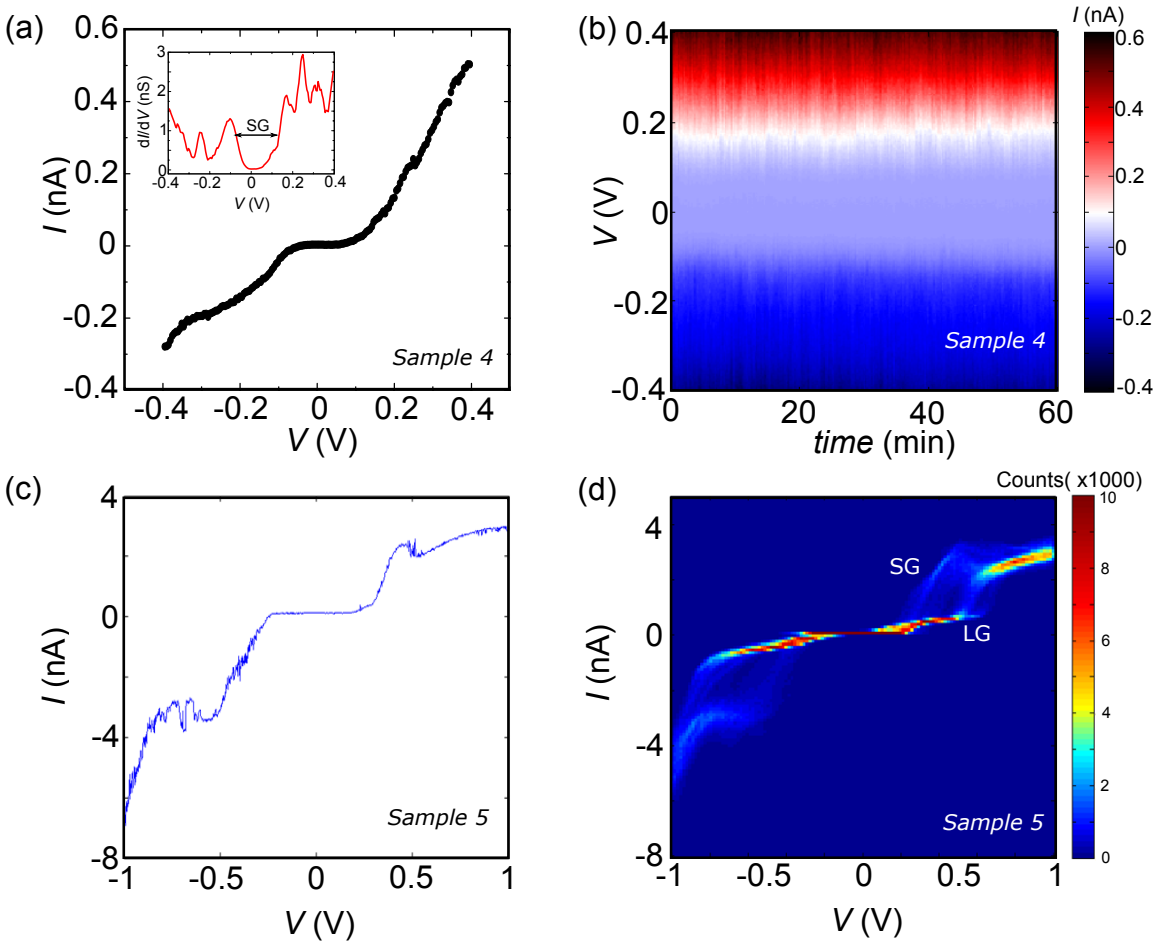

Figure S3: (a) I versus V measured in sample 4 at $T = 100$ K. The inset shows the differential conductance $\mathrm{d}I/\mathrm{d}V$ numerically derived from I. The conductance gap is consistent with a SG state. (b) Color plot of I measured as a function of V and time. No conductance bistability or switching to a LG state is observed. (c) I versus V measured in sample 5. Negative differential conductance is observed symmetric in bias. (d) I versus V histogram made of 10^4 traces measured over time in sample 5. Two bistable conductance states can be observed.

with samples 1 to 3 in the main manuscript. The current level dropped around one order of magnitude between these measurements and the time trace shown in Figure 3 of the main manuscript, possibly due to a rearrangement of the molecule in the junction. Importantly, the bistable character of the molecular junction was preserved.

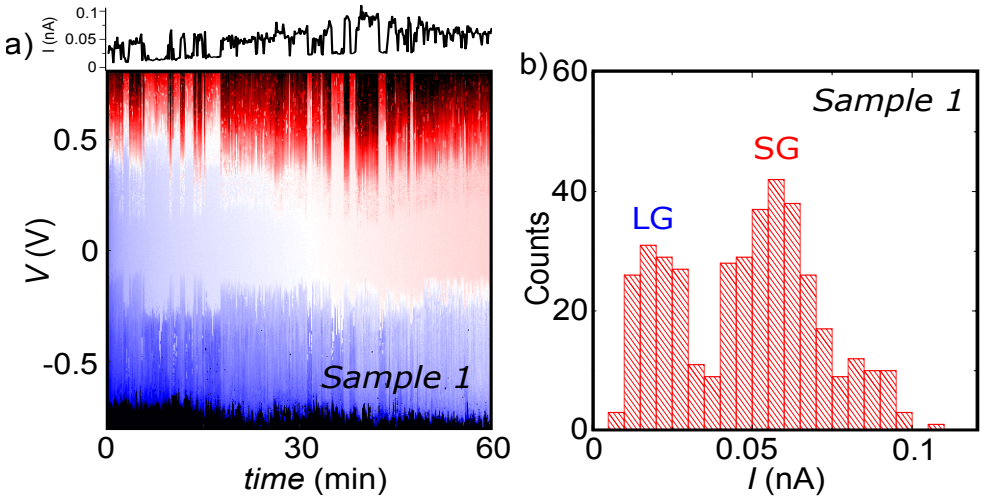

Figure S4: (a) Representative current color plot as a function of bias voltage and time measured for sample 1. The top current trace is taken from the color plot at $V = 0.48$ V. (b) Current histogram extracted from (a) at $V = 0.48$ V. The bin size is 0.005 nA and the total number of counts is 401.

Figure S4(a) shows the time dependence of the I-V characteristics of sample 1 shown in the main manuscript. A switching in time between two states, similar to the one shown in Figure 3 of the main manuscript, is observed. This is more clearly seen in the single I trace taken at $V = 0.48$ V from the plot (top of Figure S4(a)). A histogram of the current at that bias voltage is shown in Figure S4(b). Two conductance values denoted as LG and SG emerge from the noise. The high-current tails of both peaks is more extended in I, probably due to a drift of the global current to higher values as already observed in the I trace in Figure S4(a).

2.1.-Negative differential resistance

Sample 3 shows clear negative differential resistance (NDR) at positive bias. In addition, sample 5 shows symmetric NDR at positive and negative bias, as seen in Figure S3(c). This behavior has been reported for SCO molecules between gold electrodes.[4] NDR in a molecular junction is a complex phenomenon where several mechanisms could be underlying: vibrational modes, interfering transport paths within the molecule and different electrode-molecule couplings among others, see Ref.[5] and references therein for a detailed description. The transmission functions shown in Figure 4 of the main manuscript seem to discard the interference scenario since no suppression of the transmission is observed.

Additionally, in the case of graphene electrodes, it is predicted that sharp zig-zag edges could yield NDR because they carry localized edge states if contacted appropriately; other edge configurations convey trivial functionalities.[6] Interestingly, the molecular features in the conductance are predicted to be universal for graphene electrodes, in the sense that do not depend on the details of the molecule-electrode contact. This effect is due to the physisorbed nature of our contacts and has been discussed in detail in Ref.[7] . The atomic-scale shape of our graphene edges varies from device to device and therefore we expect some variability in the conductance features (like NDR) superimposed to the reproducible features stemming from the molecule (the bi-stable switch).

3. DFT calculations

3.1. Density of states in the LS and HS states

Figure S5 shows the effect of the molecular ligand field on the metallic d orbitals of the Fe(II) atom. The five d orbitals initially degenerated in the free ion are split into e_g and t_{2g} states by an octahedral symmetry. A further reduction of the ligand symmetry to S_4 splits further the levels.

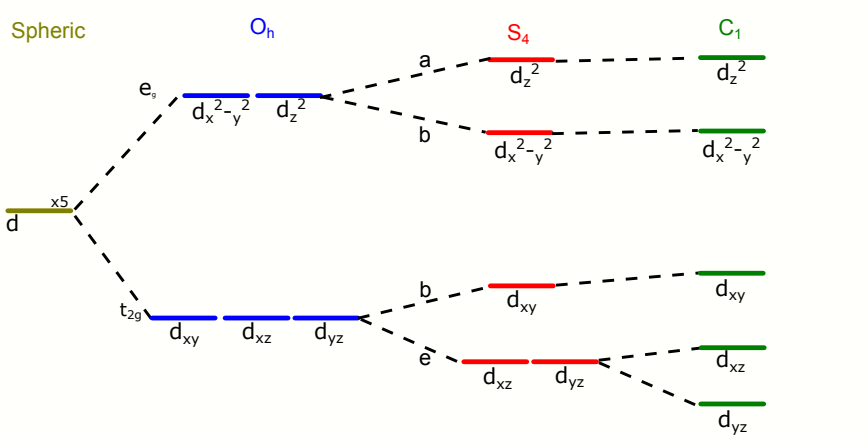

Figure S5: Components of a metallic d orbital splitting under octahedral (O_h), tetrahedral (S_4) and C_1 symmetry.

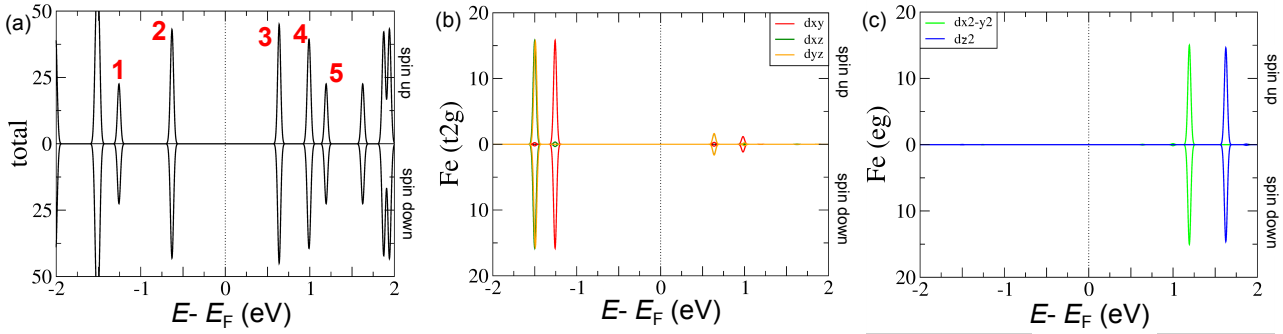

Figure S6: (a) Total projected density of states for the isolated Fe-SCO molecule in the LS state. The red numbers correspond to the states plotted in Figure S7. (b) Local projected density of states associated to the t_{2g} orbitals of Fe in the LS state. (c) Local projected density of states associated to the e_g orbitals of Fe in the LS state.

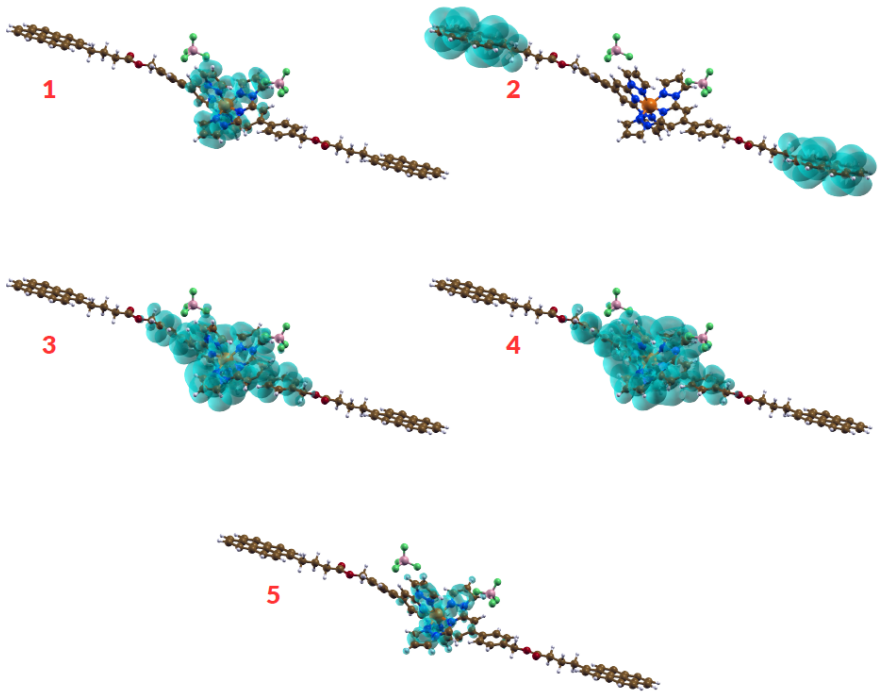

Figure S7: Local density of states of the five orbitals closer to the Fermi level for the Fe-SCO molecule in the LS state. The numbers correspond to those in Figure S6. Note that the conjugation is broken at the oxygen atoms; electron transmission through the molecule is therefore most likely facilitated by electron injection through the molecular backbone, instead of the pyrene groups as previously reported.[3]

The calculated projected density of states of the isolated Fe-SCO in the LS state is shown in Figure S6(a). As explained in the main manuscript the density of states is spin degenerate. The d_{xy}, d_{yz} and d_{xz} states (t_{2g}) lie mainly below the Fermi level while the $d_{x^2-y^2}$ and d_{z^2} states (e_g) are found well above as seen in the projected density of states in Figure S6(b) and Figure S6(c) associated to the t_{2g} and e_g states respectively. The local density of states of the orbitals closer to the Fermi level is plotted in Figure S7. The states 3 and 4, with small contributions of the t_{2g} orbitals, are strongly delocalized over the Fe-SCO core up to the oxygen atoms where the conjugation is broken. The states 1 and 5, mainly associated with the d_{xy} and $d_{x^2-y^2}$ orbitals, which are transversal to the direction of the molecule, are slightly delocalized. The main contribution of d_{yz} and d_{xz} is found well below the Fermi level and d_{z^2} is at higher energies. The state 2 is mainly delocalized over the pyrene anchoring groups.

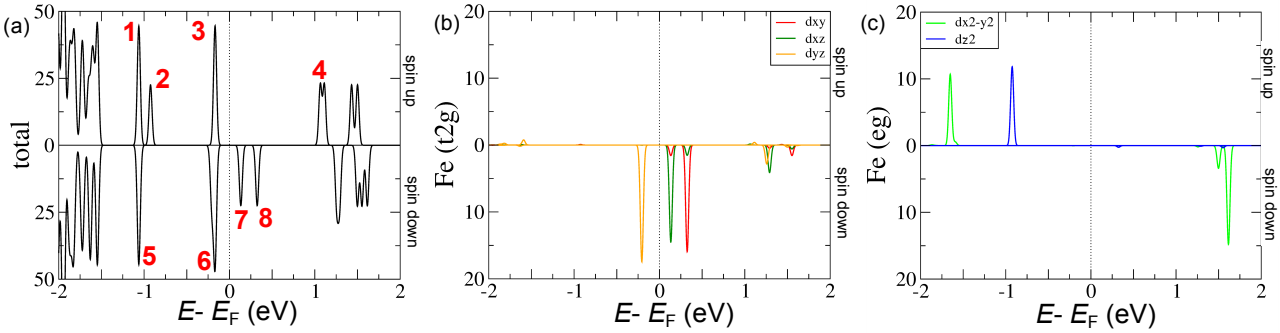

Figure S8: (a) Total projected density of states for the isolated Fe-SCO molecule in the HS state. The red numbers correspond to the states plotted in Figure S9. (b) Projected density of states associated to the t_{2g} levels of Fe in the HS state. (c) Projected density of states associated to the e_g levels of Fe in the HS state.

The magnetic behavior of the Fe-SCO in the HS state is rather different. The calculated projected density of states of the isolated Fe-SCO in the HS sate is shown in Figure S8(a). The density of states is now spin resolved. Both the t_{2g} and e_g orbitals are occupied and well below the Fermi level for the majority spin component, while only d_{yz} from the t_{2g} orbitals is occupied for the minority spin component (see Figure S8(b) and S8(c)). The minority spin t_{2g} states are only partially occupied, and this fact leads them to be placed quite close

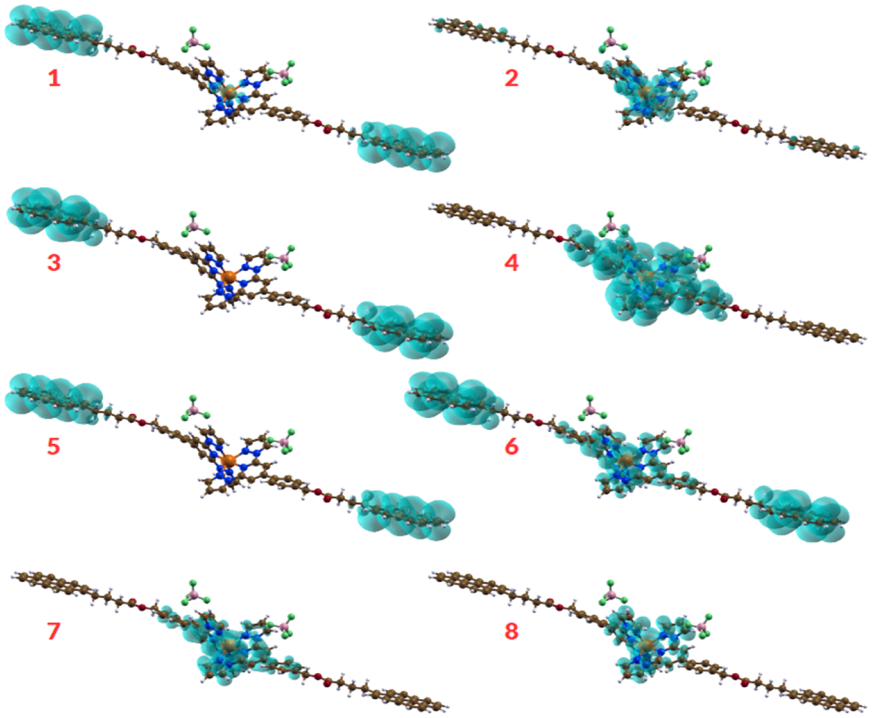

Figure S9: Local density of states of the seven orbitals closer to the Fermi level for the Fe-SCO molecule in the HS state. The numbers correspond to those in Figure S8

to the Fermi level. Indeed, as the symmetry of the Fe-SCO is reduced from O_h to S_4, the e_g states split into a and b states, and the t_{2g} split into b and e states as seen in Figure S5. The doubly-degenerate states are further split by a Jahn-Teller distortion. Because these turn out to be the two states lying closest to the Fermi energy, this final splitting has a strong impact on $T_\downarrow$ around the Fermi level. As a result of the orbital filling, the spin up transmission is mainly blocked up to high energies and only the spin down is transmitted, as explained in the main manuscript. The molecule could therefore be used as a spin filter up to relatively high energies.

The local density of states of the orbitals closer to the Fermi level is plotted in Figure S9. The 2, 6, 7 and 8 states corresponding to d_{z^2}, d_{yz}, d_{xz} and d_{xy} respectively, are slightly delocalized around the Fe core. State 4, with a very small contribution of d_{yz} is very delocalized in the central part of the molecule up to the oxygen atoms. The main contribution of $d_{x^2-y^2}$ lies at higher absolute energies above and below the Fermi level. The states 1, 3

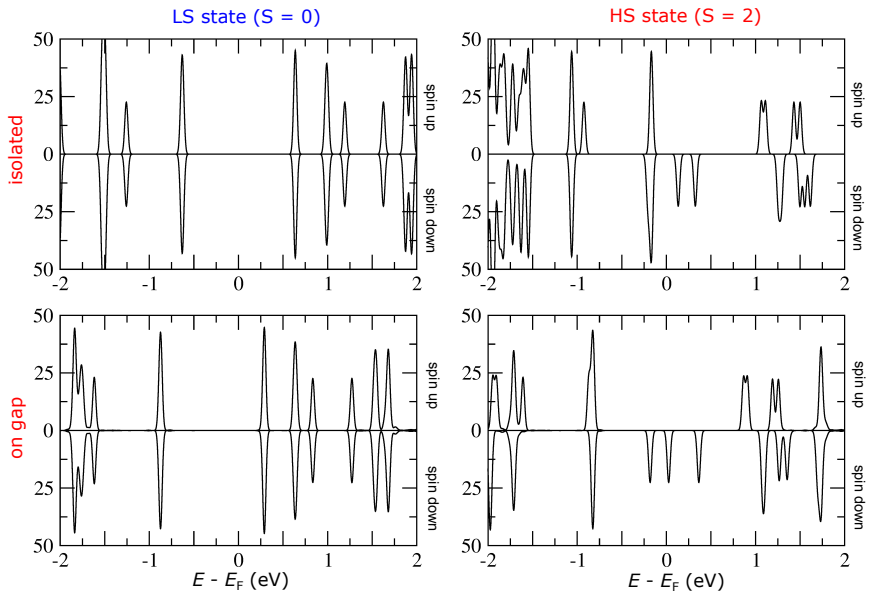

Figure S10: Comparison of the total projected density of states for the isolated molecule and the molecule deposited on the gap in the HS and LS states. The molecular orbitals associated to Fe undergo mainly a rigid displacement in energy.

and 5 are mainly present in the pyrene anchoring groups.

The discussion and conclusions derived for the isolated molecule can be applied to the molecule placed linking the graphene electrodes. The main effect of the electrodes is a rigid shift of the molecular orbitals associated to the Fe to lower energies as shown in the comparative Figure S10.

3.2. Current switching mechanism and transition rates

We have identified two possible sources of the Low to High Conductance switching, both due to Franck-Condon physics. The first (FCI) is the conventional switching mechanism for Fe(II) spin crossover molecules, where the ground state switches between S=0 and S=2 multiplets due to Temperature, light or perhaps the voltage.[8] The second corresponds to sequential ($N \rightleftharpoons N+1$) or cotunneling ($N \rightleftharpoons N$) Franck-Condon physics (FCII),[9,10] corresponding to $S = 0 \rightleftharpoons S = 1/2$ or $S = 2 \rightleftharpoons S = 3/2$, respectively.

To try and shed some light on this issue we plot in Figure S11 the relative energy of

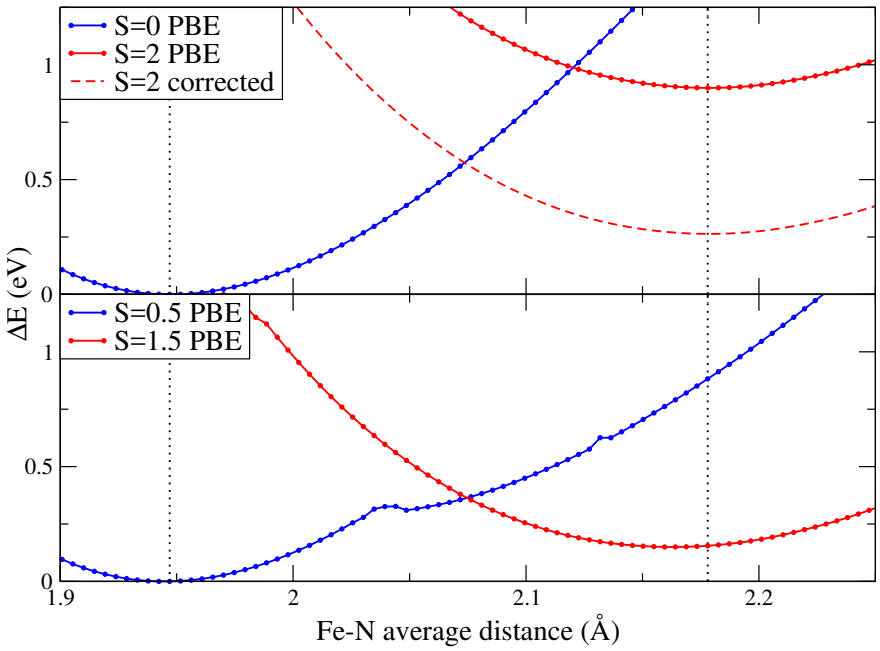

Figure S11: Energy difference between different spin states as a function of the Fe-N distance for the system with N (top) and $N+1$ (bottom) electrons.

the different spin solutions for the system with N (top) and $N+1$ (bottom) electrons, for structural solutions ranging between the ground state of the $S=0$ and the $S=2$ systems. The extra electron of the $N+1$ systems is located in a molecular orbital with contribution from the central Fe ion, thus the spin solutions correspond to the distribution of 7 d electrons distributed in a strong ($S=0.5$) or weak ($S=1.5$) O_h (or close to O_h) ligand field. We find that the Fe-N bond distance does not change by adding an extra electron. Therefore, the Franck-Condon factor for $N \rightleftharpoons N+1$ sequential tunneling is close to 1. This means that Franck-Condon blockade is not the dominant mechanism, so the FCII scenario is ruled out. On the other hand, there is a strong difference in the Fe-N bond distance of the $S=0$ and $S=2$ systems indicating a strong spin-phonon coupling. This fact implies that Franck-Condon factors for spin-switching are small as usually happens with Fe(II) SCO molecules. We analyse therefore whether the FCI scenario fits with our experiments.

Literature tells that Fe-Terpyridine molecules tend to show slower switching times than other Fe(II) SCO molecules, and that those switching times are temperature-independent up to higher threshold temperatures.[8,11] We borrow the transition rate discussion for $S=$

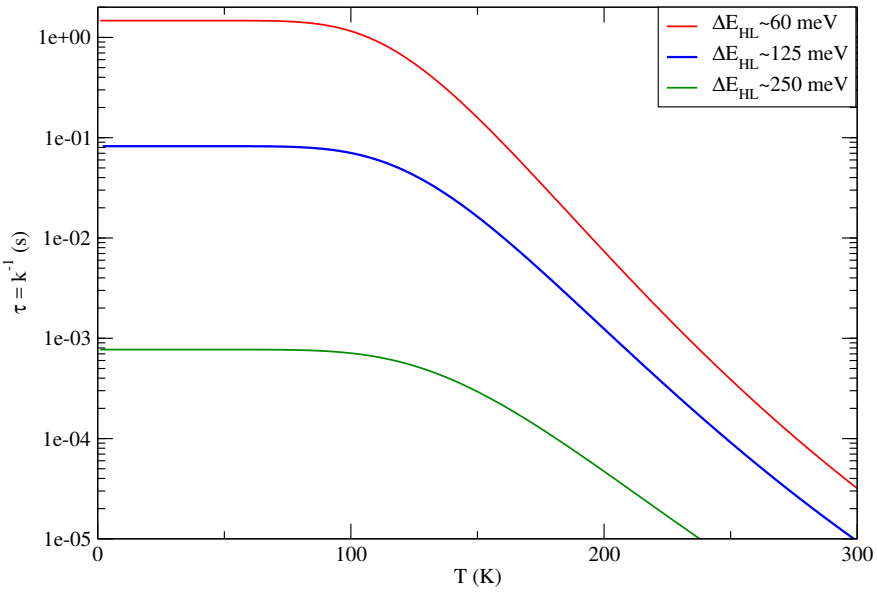

Figure S12: Average lifetime τ of the spin states as a function of the temperature for different values of ΔE_{HL}

$0 \rightleftharpoons S = 2$ switching from Buhks *et al.*[8] :

$$k = \frac{2\pi}{\hbar} V_{SO}^2 \, G \tag{S1}$$

where V_{SO} indicates the second order transition between electronic states of $S = 0$ and $S = 2$ due to the spin-orbit coupling and G is the Franck-Condon factor which measures the vibrational overlap. To give rough numbers, we use the energy difference between the $S = 2$ and $S = 0$ ground states ΔE_{LH}, that we extract from our DFT GGA calculations; we find it to be 900 meV (7260 cm^{-1}). However, we note that DFT GGA calculations are known to overstabilize the LS state, thus overestimating ΔE_{LH}. Indeed, our multielectronic calculations of the core Fe^{2+} levels give an estimate ΔE_{LH} ~250 meV (2000 cm^{-1}). So we have decided to shift the two parabolae in Figure (S11) accordingly. We can also estimate from the curvature of the two parabolae an elastic constant $K = 240$ N/m. The corresponding vibrational energy is $\hbar\omega$=67 meV (537 cm^{-1}). From these parameters we calculate the transition rate as a function of the temperature in Fig. (S12). For our estimated value of ΔE_{HL} ~250 meV we find a constant transition rate up to more than 100 K, with a value of

τ $\sim$$10^{-3}$ s. This transition rate can be strongly modified if the deposition of the molecule modifies the energy difference between spin states to ΔE_{HL} $\sim$125 meV (τ $\sim$$10^{-1}$ s) or ΔE_{HL} $\sim$60 meV (τ $\sim$1 s), for example. Other factors, such as the changes in the vibrational states due to the deposition of the molecule, can also play a role.

References

(1) Island, J. O.; Holovchenko, A.; Koole, M.; Alkemade, P. F. A.; Menelaou, M.; Aliaga-Alcalde, N.; Burzurí, E.; van der Zant, H. S. J. *J. Phys. Condens. Matter* **2014**, *26*, 474205.

(2) Perrin, M. L.; Burzurí, E.; van der Zant, H. S. J. *Chem. Soc. Rev.* **2015**, *44*, 902–19.

(3) Burzurí, E.; Island, J. O.; Díaz-Torres, R.; Fursina, A.; González-Campo, A.; Roubeau, O.; Teat, S. J.; Aliaga-Alcalde, N.; Ruiz, E.; van der Zant, H. S. J. *ACS Nano* **2016**, *10*, 2521–2527.

(4) Harzmann, G. D.; Frisenda, R.; van der Zant, H. S. J.; Mayor, M. *Angew. Chemie Int. Ed.* **2015**, *54*, 13425–13430.

(5) Perrin, M. L.; Frisenda, R.; Koole, M.; Seldenthuis, J. S.; Celis Gil, J. A.; Valkenier, H.; Hummelen, J. C.; Renaud, N.; Grozema, F. C.; Thijssen, J. M.; Dulić, D.; van der Zant, H. S. J. *Nat Nano* **2014**, *9*, 830–834.

(6) Carrascal, D.; García-Suárez, V. M.; Ferrer, J. *Phys. Rev. B* **2012**, *85*, 195434.

(7) García-Suárez, V. M.; Ferradás, R.; Carrascal, D.; Ferrer, J. *Phys. Rev. B* **2013**, *87*, 235425.

(8) Buhks, E.; Navon, G.; Bixon, M.; Jortner, J. *Journal of the American Chemical Society* **1980**, *102*, 2918–2923.

(9) Burzurí, E.; Yamamoto, Y.; Warnock, M.; Zhong, X.; Park, K.; Cornia, A.; van der Zant, H. S. J. *Nano Lett.* **2014**, *14*, 3191–6.

(10) Koch, J.; von Oppen, F.; Andreev, A. V. *Phys. Rev. B* **2006**, *74*, 205438.

(11) Rudavskyi, A. Spin crossover mechanisms unravelled by theory. Ph.D. thesis, Zernike Institute for Advanced Materials, University of Groningen, the Netherlands, 2014.